Thin-Walled Structures 191 (2023) 111041

Contents lists available at ScienceDirect

Thin-Walled Structures

journal homepage: www.elsevier.com/locate/tws

Full length article

On the winding pattern influence for filament wound cylinders under axial compression, torsion, and internal pressure loads

Eduardo A.W. de Menezes [a], Tales V. Lisbôa [a], José Humberto S. Almeida Jr. [b,*], Axel Spickenheuer [a], Sandro C. Amico [c], Rogério J. Marczak [d]

[a] Department of Materials Engineering, Leibniz Institute for Polymer Research, Hohe Straße 6, Dresden, 01069, Germany
[b] School of Mechanical and Aerospace Engineering, Queen's University Belfast, Stranmillis Road, Belfast, BT9 5AH, United Kingdom
[c] Department of Materials Engineering, Federal University of Rio Grande do Sul, Avenida Bento Goncalves 9500, Porto Alegre, 90650-001, Brazil
[d] Department of Mechanical Engineering, Federal University of Rio Grande do Sul, Rua Sarmento Leite 425, Porto Alegre, 90050-170, Brazil

ARTICLE INFO

Keywords:
Winding pattern
Numerical modelling
Composite cylinders
Filament winding

ABSTRACT

An intrinsic characteristic of components manufactured by the filament winding process is a winding pattern formation during the processing. This paper aims at unlocking and understanding how the winding pattern influences the mechanical behaviour of filament wound cylinders under different boundary conditions. To realize this, a series of finite element models followed by an original geometric approach to generate the pattern are herein developed. Four different patterns and six different winding angles are modelled. These are also modelled by varying the number of layers towards understanding whether there is a correlation between the pattern and the number of layers or not. Three loading cases are considered: axial compression, pure torsion, and internal pressure. Key results reveal that the more layers are stacked to the cylinder, the less impactful is the winding pattern to all loading cases herein investigated.

1. Introduction

In the filament winding (FW) process, when considering helical and polar winding trajectories, continuous fibres are wound around a rotative mandrel from one end – half cycle – to the other – full cycle. The filament angle inverts when changing from forward to backward movement, producing interlaced layers [1]. This winding angle, α, is defined by the ratio between the deposited tow and the longitudinal axis of the mandrel [2]. As usual for laminated composites with continuous fibres, the mechanical behaviour of a filament wound structure is strongly dependent on the winding angle given the anisotropy of the fibres [3–9]. The combination of rotational and axial movements along with the continuity of the manufacturing process create a repetitive pattern, leading to a mosaic arrangement of diamond shapes on the surface [10–12]. The number of diamond shapes along the circumferential direction is an integer number referred to as the winding pattern (*WP*) [2,10,11,13]. The influence of the *WP* on the mechanical behaviour of filament wound components is still not fully comprehended. Table 1 reports the state of the art on this subject.

Filament wound cylinders under axial compression were experimentally tested by Claus [14] wherein he observed that diamond shape lengths matching buckling modes should be avoided since they create regions more susceptible to this failure mode. Despite following this observation for the buckling behaviour, Hahn et al. [15] concluded that the *WP* has no correlation with the axial stiffness of the cylinders in axial compression. In their experiments, Azevedo et al. [11] included the ageing effect with distilled and seawater, observing a slight influence in axial stiffness, but more pronounced in strength limits. In the numerical field, Guo et al. [20] reported a difference of 4% in strength when changing the *WP* from 4 to 10. Also considering failure by buckling, external pressure models were elaborated by Guo et al. [20], which reported a difference of around 1% with the same 4–10 pattern range. Moreno et al. [17] conducted experimental tests, and could not observe differences in the structure's strength. Morozov [10] and Mian [18] carried out numerical models simulating internal pressure, both having a single-layer filament wound cylinder, and reported a difference of more than 30% in developed stresses within the considered pattern range. On the experimental field, Rousseau et al. [16] measured a much lower influence of the pattern on the strength and a negligible influence on the stiffness. Regarding axial tension, different *WP* were tested by Rousseau [16] and Wen et al. [19]. Despite the high standard deviations, both works showed a decrease in strength as the *WP* increased. Regarding axial stiffness, the *WP* showed a negligible effect.

More recent works addressed the *WP* role in mechanical behaviour, aiming at a more challenging boundary condition [13,21–23]. Radial compression tests demand more degrees of freedom to be controlled,

* Corresponding author.
E-mail address: humberto.almeida@qub.ac.uk (J.H.S. Almeida Jr.).

https://doi.org/10.1016/j.tws.2023.111041
Received 30 January 2023; Received in revised form 2 June 2023; Accepted 17 July 2023
Available online 4 August 2023

Table 1
State-of-the-art on winding patterns effects on filament wound cylinders depicting the load case, approach, number of layers N, WP investigated, and the output. The symbol "✓" means influential, whereas the symbol "✗" means negligible influence.

Author(s)	Load case	Approach	N	*WP*	Stiffness	Stress/Strength
Claus (1992) [14]	Axial compression[a]	Experimental	–	–	✓	✓
Hahn et al. (1994) [15]	Axial compression[a]	Experimental	1	1–26	✗	✓
Rousseau (1999) [16]	Axial tension	Experimental	6	2–11	✗	✓
	Internal pressure	Experimental	6	2–11	–	✓
Morozov (2006) [10]	Internal pressure	Numerical	1	2–8	–	✓
Moreno et al. (2008) [17]	External pressure[a]	Experimental	7	1–5	–	✗
Mian et al. (2011) [18]	Internal pressure	Numerical	1	2–8	–	✓
Wen et al. (2013) [19]	Axial tension	Experimental	7	1–5	–	✓
Azevedo et al. (2020) [11]	Axial compression[a]	Experimental	1	1–5	✓	✓
Guo et al. (2020) [20]	Axial compression[a]	Numerical	7	4–10	–	✓
	External pressure[a]	Numerical	7	4–10	–	✓
Lisbôa (2020) [13]	Radial compression	Experimental	1	1–10	✗	✓
Stabla et al. (2021) [21]	Radial compression	Numerical	1	2–7	✓	✓
Stabla et al. (2022) [22]	Radial compression	Experimental	1	1–3	✓	–
Lisbôa et al. (2022) [23]	Radial compression	Numerical	1	1–3	–	✓

[a]Buckling failure mode

and numerical models might require incorporating nonlinear displacement hypotheses. With respect to strength, Stabla et al. [21] found divergences between numerical and experimental responses. The authors attributed them to differences in thickness and degrees of coverage among the specimens. A wider *WP* range was experimentally investigated by Lisbôa et al. [13], where samples with higher *WP* showed more strength and negligible deviations in stiffness. Stabla et al. [22] investigated both *WP* and α, and they found out that the influence of the *WP* on stiffness changes according to α.

The strategy commonly adopted in numerical works herein reported consists in dividing the cylinders into triangular mosaic shapes, attributing $-\alpha$ and $+\alpha$ angles to each mosaic. Shell elements are used to build different laminates for each stacking sequence, leading to an abrupt change in material properties when crossing the periphery of these mosaic shapes. This procedure is straightforward for a single-layer cylinder, but its complexity harshly increases when dealing with multi-layered structures, where the intersection of the mosaic shapes of every layer must be taken into account to build laminates with correct stacking sequences over the entire length. Despite the different conclusions in the works mentioned above, it has been numerically shown and through digital image correlation (DIC) [24] that stress concentrations occur in this periphery and in the interweaving regions (regions where $-\alpha$ and $+\alpha$ plies cross themselves), leading to potential failure [25]. However, by adding more layers, the pattern effect reduces [10].

From the state-of-the-art presented in Table 1, it is yet to be understood whether the *WP* influences or not the performance of composite cylinders under certain loading conditions. Moreover, no study reports a correlation among the *WP*, the winding angle, and the number of layers. Experimentally speaking, it is challenging to observe that influence since, when they are varied, other parameters (e.g., degree of coverage, fibre compaction) also change, and these variations disturb the pattern analysis. Analogously, in the numerical field, it is necessary to control as many parameters as possible related to geometry generation, including mesh effects, initial winding angles, and symmetries, to mitigate their effect on the analysis and focus solely on the pattern influence.

This paper then focuses on developing a series of finite element (FE) models to unveil the influence of the winding pattern on the mechanical performance of filament-wound composite cylinders under axial compression, external pressure, and pure torsion loading cases. Furthermore, the effect of stacking layers and the winding angle are also investigated to quantify the contribution of the *WP* and how they correlate. A detailed description of the geometrical approach to constructing the winding pattern is also presented in detail.

2. The finite element modelling

2.1. The winding pattern generation

A geometric approach was developed to construct the pattern onto the cylinder [23]. This is then implemented into Ansys Parametric Design Language (APDL) [26]. A key advantage of this tool is that the mesh can be coupled with the geometric entities, making the procedure "mesh independent", i.e., the refinement of the mesh has no influence on the pattern regions.

The *WP* is a diamond-shaped structure that occurs on the peripheric surface of the cylinder due to the kinematics of the process. Fig. 1 presents schematic views of the *WP*, highlighting its regions: regular laminate (RL), circular cross-over (CCO or zig-zag), and helical cross-over (HCO) [2]. The RL defines the region where no interweaving is observable. The CCO region and HCO are areas where interweaving takes place. Here, the zig-zag line in the CCO region, depicted in Fig. 1(a), is simplified by a straight line, illustrated by the dashed line in the central diamond. Also, the stacking configuration of a double layer is illustrated in Figs. 1(b), while at the bottom part is a photo of the periphery of a filament wound cylinder. The sector and the height define the diamond size in the circumferential (θ) and axial (z) directions, respectively.

Fig. 2 schematically describes the procedure of constructing a multi-layered geometry. Initially, an algorithm for developing the *WP* in one double layer is derived. This algorithm constructs the diamond-shaped structures around the reference cylinder (dimensions of the mandrel) taking into account the *WP* and α [13,23]. With the first, the sector (circumferential direction) of each diamond is defined whereas with the second its height (axial direction) is determined. The resultant geometric model for a double layer is shown in Fig. 2(a) for three different examples: (top) WP=1 and $\alpha_1 = 60°$; (middle) WP=4 and $\alpha_2 = 45°$; and (bottom) WP=5 and $\alpha_3 = 15°$.

For the construction of the multi-layered geometric model, Boolean operations over the areas of each double layer are applied. These operations are simply multiple area intersection procedures in which the proper stacking configuration is sought. The first layer (top) is selected as a base for each stacking, and the intersections with the second layer (middle) are verified. The resultant generates 4 different stacking configurations. This new cylinder is then taken as a base and new Boolean operations are performed with the third layer (bottom), resulting in 8 different configurations. The number of different stacking is 2^N, where N defines the number of layers. The operations must follow a sequential way, similar to the manufacturing process, thus the procedure produces proper stacking.

Despite not being a restriction of the modelling approach, for the sake of simplicity, an anti-symmetric plane is constructed: in Fig. 2,

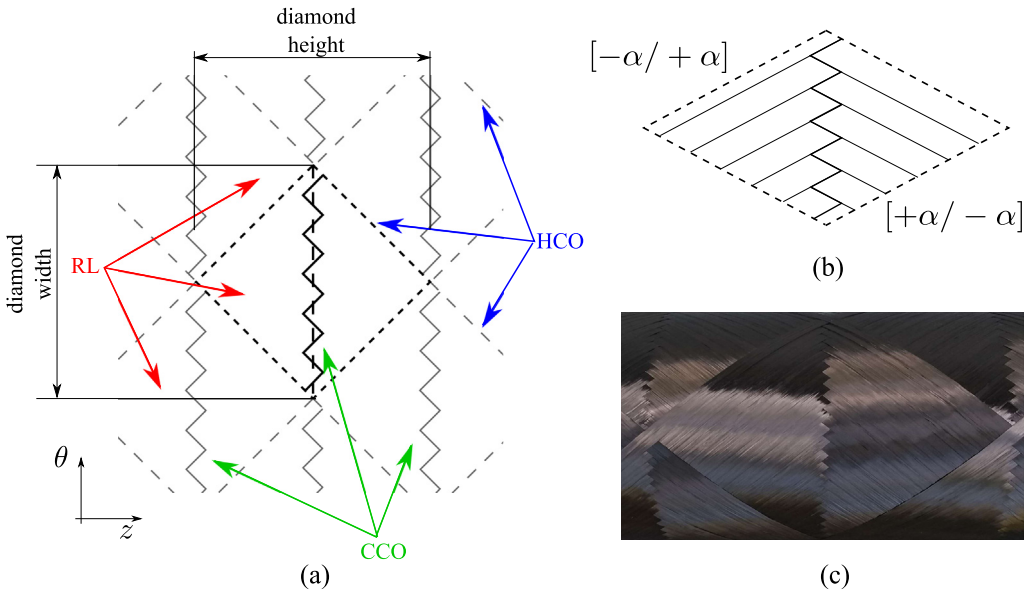

Fig. 1. (a) Scheme of the regions of a *WP* highlighting a single diamond in the centre. (b) Representation of the stacking and (c) a photo of the peripheral surface of a filament wound cylinder.

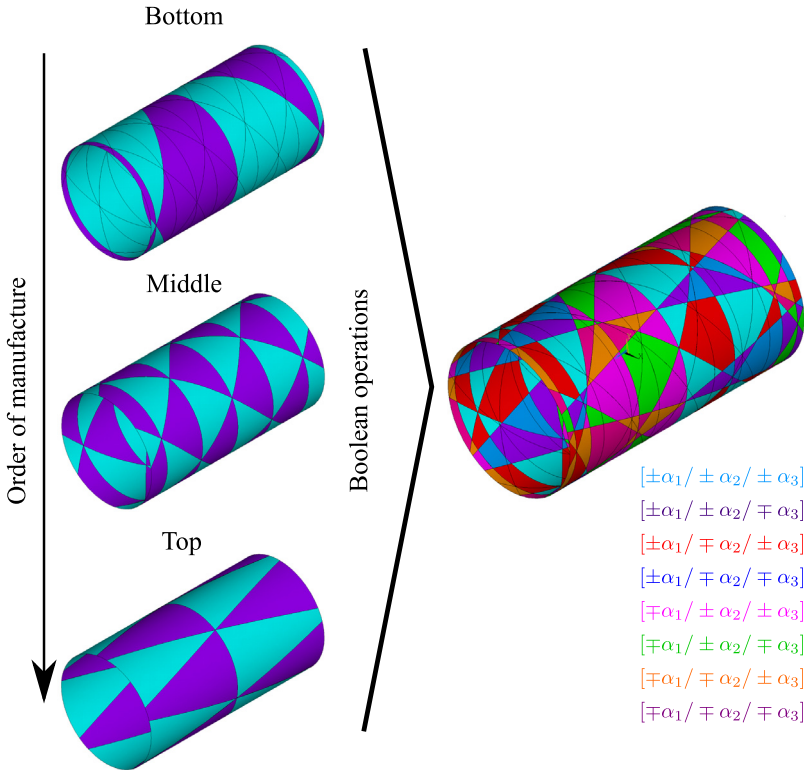

Fig. 2. Example of construction of a multi-layered cylinder considering the *WP* information of each layer. On the left, light blue and purple are $[\pm\alpha_i]$ and $[\mp\alpha_i]$ layers, respectively. From the top to bottom, the cylinders have (top) *WP*=1 and $\alpha_1 = 60°$; (mid) *WP*=4 and $\alpha_2 = 45°$; and (bottom) *WP*=5 and $\alpha_3 = 15°$. On the right, are the three double-layered cylinders with 8 different stacking configurations.

one can observe an "inverse" stacking from the middle of the cylinder. This position is then considered as $z = 0$. Moreover, a reference angle ϕ is defined for each double layer. This angle simply determines a shift on the first sector to be constructed, so that identical angles and patterns could be developed without the diamonds-shaped structure falling one over another. More examples are shown in Section 3.

The FE mesh is populated with shell elements. In order to avoid any kind of forces being applied away from the mid-surface, the reference surface (the mandrel) is offset to the mid-surface, considering the thickness of each layer. The scheme of the cross-section is shown in Fig. 3, where R_i, R_{ms}, and R_o correspond to inner, mid-section, and outer radii, respectively, while L defines the cylinder length. Both global (r, θ, z) and local $(1, 2, 3)$ coordinate systems are also illustrated in Fig. 3. The local coordinates follow the fibre direction: 1 is tangent to the fibre (direction of α); 2 is perpendicular to 1 and in the tangent plane of the cylinder outer surface, and 3 is parallel to the aforementioned plane.

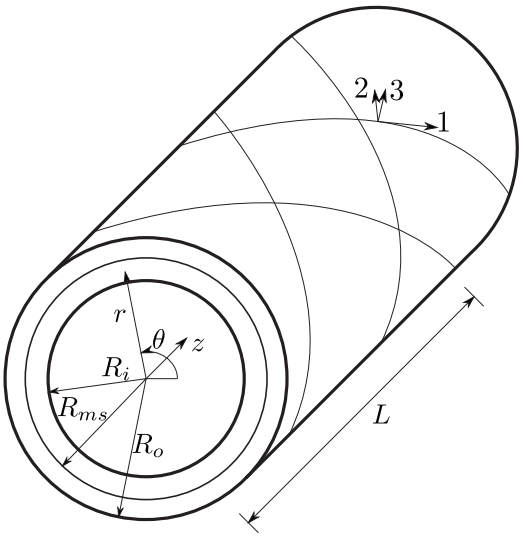

Fig. 3. Scheme of the cross-section of the cylinder.

2.2. The input parameters

Typical elastic properties of a carbon fibre-reinforced polymer composite are adopted for all the analyses. The longitudinal (E_1) and transverse (E_2) elastic moduli are 139.90 GPa and 8.52 GPa, respectively. Both the in-plane (G_{12}) and out-of-plane shear (G_{13}) moduli are 4.26 GPa, and the in-plane (ν_{12}) and out-of-plane (ν_{13}) Poisson ratios are 0.26. Since out-of-plane properties are of minor importance in the present work, they are assumed equal to their equivalent in-plane value. Regarding geometrical parameters, L and R_i are constant, being, respectively, 240 mm and 68 mm, while R_{ms} and R_o are dependent on the total number of layers N, where each layer consists of a forward stroke followed by a backward stroke. Hence, the thickness, t, is evaluated through

$$t = 2hN \tag{1}$$

where h is the tow thickness, herein considered 0.25 mm, i.e., the total thickness of each double layer is 0.5 mm. Both L and R_i are carefully chosen to avoid intersection between the diamond-mosaic shapes close to the cylinder edges, so as to circumvent any excessive element distortions that might occur in this region. The reference angle, ϕ, of the ith layer is computed through

$$\phi_i = (i-1)\frac{360^\circ}{N} \quad [\text{deg}]. \tag{2}$$

which means that for most of the cases herein evaluated the pattern is equally distributed around the surface of the mandrel. This should be considered as a simplification of the problem in analysis: with this arrangement, it is easy to track any influence/modification that is due to the pattern.

To investigate the cross-influence of *WP* and *N* in the mechanical behaviour of the cylinders, the analyses here are carried out under different combinations of *N* (1, 2, 4, and 6) and *WP* (0, 1, 3, 5, 7). The $WP = 0$ is the reference configuration, where the cylinder is simply extruded with $-\alpha$ and $+\alpha$ layers, therefore, neglecting the pattern effect. To verify the consistency and validity of the achieved results, a wide range of winding angles is tested (15°, 25°, 35°, 45°, 55°, and 65°). The developed cylinder views are shown in Fig. 4 to illustrate the applied winding patterns and angles. Moreover, Table 2 shows the θ-position (refer to Figs. 1,3), where the change from one diamond shape to another occurs, creating the interweaving region (the boundary between black and grey triangles in Fig. 4).

In contrast with α, the investigated ranges for *N* and *WP* are more limited. The former is designed to keep the thickness effect negligible when comparing different configurations, while the second aims to keep large enough diamond-mosaic shapes, originating from the *WP*, yielding smoother stress gradients and allowing a more accurate computation of stresses. Furthermore, as the first step, the analyses will cover only the linear response of the cylinders.

A fine mesh is required to compute the stress oscillations developed in the cylinder and capture the transition in the mechanical behaviour over the different regions along the layers. Meshes are built with a quadratic Serendipity shell element (SHELL281 - ANSYS reference) in its degenerate form (triangle) [23], due to the winding pattern and geometry. The element section has nine integration points, equally spaced through-thickness, and the offset is made from the mid-section radius R_{ms}. The FE mesh has a total of 450 elements along the circumferential direction.

The colours in Fig. 2 represent different stacking configurations: on the left, two stacking sets; on the right, eight. The FE software considers the equivalent layer theory, which homogenizes the plies into one anisotropic layer. Thus, each colour of Fig. 2 represents one equivalent layer. At the contour lines of these layers, the nodes belong to two or more different stacking sets, which might create some mild stress concentrations at those locations.

2.3. Loads and boundary conditions

After the winding pattern is generated and implemented into the FE environment, loads and boundary conditions (BCs) can then be applied. Three loading cases are considered: axial compression (Fig. 5(a)), torsion (Fig. 5(b)), and internal pressure (Fig. 5(c)). For axial compression, target stress of $\sigma_z = 500$ MPa is considered. This procedure eases the comparison among different patterns and stacking configurations. Hence, the axial load is equivalent to this stress multiplied by the cross-section area A_c (which varies according to N). This load is applied to a master node, coupled with the u_z DOFs (degrees of freedom) of all nodes (see Fig. 5). To allow free expansion/contraction, avoiding also stresses concentrations at the ends, the displacement in u_r is not constrained, while all rotations ψ_i and u_θ are constrained on both edges (hard boundary conditions [27]). Axial displacement u_z is constrained only on the right end. These conditions impose a constant axial displacement on the left end and are depicted in Fig. 5(a).

Regarding the torsion model, the same target stress $\sigma_\theta = 500$ MPa is achieved by applying nodal forces in the circumferential direction. As in the previous loading condition, this force is computed considering A_c and applied on a master node, coupled with all nodes in the left end regarding u_θ. While the left edge is constrained only in the DOFs ψ_r and ψ_θ, the right edge is constrained also in u_θ and u_z. These boundary conditions are illustrated in Fig. 5(b).

The third case represents cylinders in internal pressure P_i, where the required value to reach circumferential stress (hoop stress) of 500 MPa is computed through membrane theory, following Eq. (3). The load is applied to the entire internal surface. To achieve a stress state as close as possible to pure hoop stress, u_z displacement is constrained only in the right end. Both ends are constrained in the DOFs u_θ, ψ_z, and ψ_θ. The BCs are shown in Fig. 5(c).

$$P_i = \frac{t \cdot \sigma}{R_{ms}} \tag{3}$$

Since geometrical nonlinearities are neglected, the stiffness K in the axial compression and torsional load cases is directly evaluated from the applied force/moment at the master node divided by the displacement/rotation where this node is coupled (left edge of the cylinders in Fig. 5(a),(b)). Stresses are evaluated considering the local coordinate system (see Fig. 3). They are computed along a circular perimeter around every 3° (120 measurements), in three different locations along the length:

- in the centre line (CL), which is in the CCO line at the coordinate $z = 0$ mm;

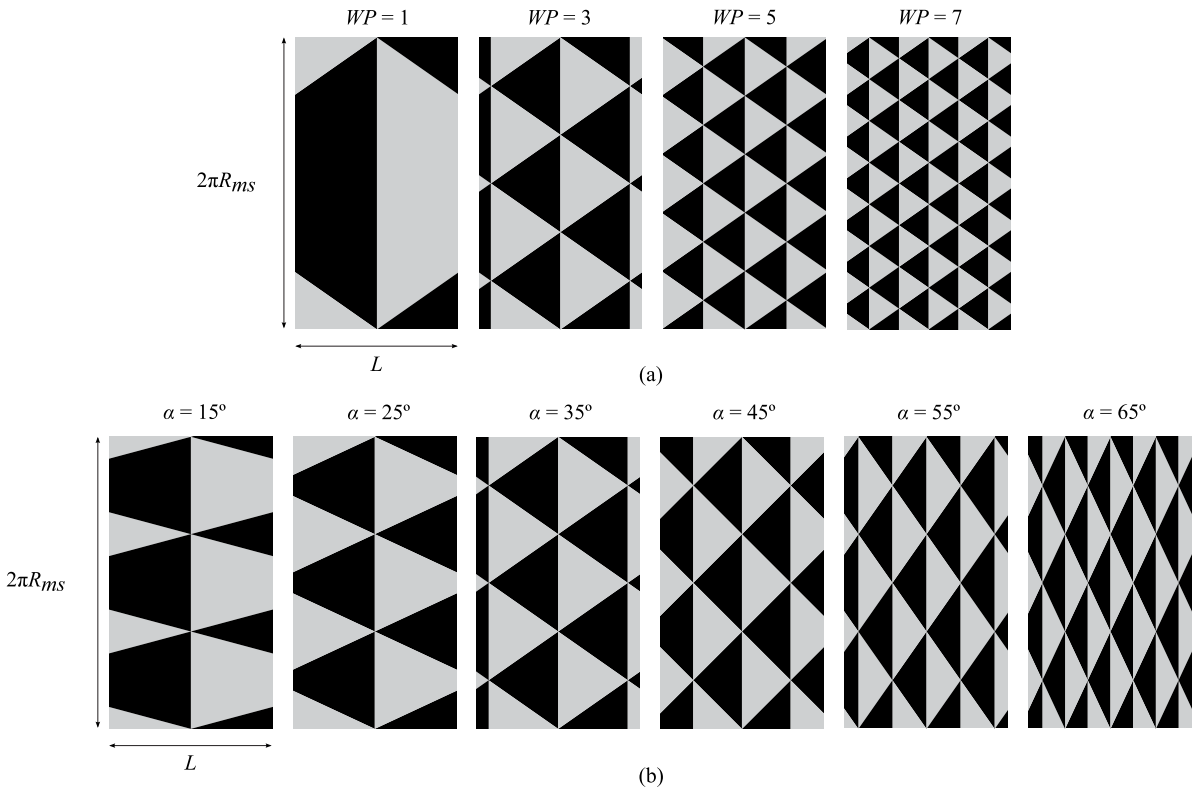

Fig. 4. The developed cylinder view showing (a) the different *WPs* applied in the present work, considering a $\alpha = \pm 35°$, and (b) the different winding angles, considering a $WP = 3$.

Table 2
Sector and reference angle, ϕ_i, between two diamond shapes along the interweaving region for different patterns and layers.

N	1	2		4				6					
ϕ_i (°)	0.0	0.0	180.0	0.0	90.0	180.0	270.0	0.0	60.0	120.0	180.0	240.0	300.0
$WP = 1$	180.0	180.0	0.0	180.0	270.0	0.0	90.0	180.0	240.0	300.0	0.0	60.0	120.0
	60.0	60.0	240.0	60.0	150.0	240.0	330.0	60.0	120.0	180.0	240.0	300.0	0.0
$WP = 3$	180.0	180.0	0.0	180.0	270.0	0.0	90.0	180.0	240.0	300.0	0.0	60.0	120.0
	300.0	300.0	120.0	300.0	30.0	120.0	210.0	300.0	0.0	60.0	120.0	180.0	240.0
	36.0	36.0	216.0	36.0	126.0	216.0	306.0	36.0	96.0	156.0	216.0	276.0	336.0
	108.0	108.0	288.0	108.0	198.0	288.0	18.0	108.0	168.0	228.0	288.0	348.0	48.0
$WP = 5$	180.0	180.0	0.0	180.0	270.0	0.0	90.0	180.0	240.0	300.0	0.0	60.0	120.0
	252.0	252.0	72.0	252.0	342.0	72.0	162.0	252.0	312.0	12.0	72.0	132.0	192.0
	324.0	324.0	144.0	324.0	54.0	144.0	234.0	324.0	24.0	84.0	144.0	204.0	264.0
	25.7	25.7	205.7	25.7	115.7	205.7	295.7	25.7	85.7	145.7	205.7	265.7	325.7
	77.1	77.1	257.1	77.1	167.1	257.1	347.1	77.1	137.1	197.1	257.1	317.1	17.1
	128.6	128.6	308.6	128.6	218.6	308.6	38.6	128.6	188.6	248.6	308.6	8.6	68.6
$WP = 7$	180.0	180.0	0.0	180.0	270.0	0.0	90.0	180.0	240.0	300.0	0.0	60.0	120.0
	231.4	231.4	51.4	231.4	321.4	51.4	141.4	231.4	291.4	351.4	51.4	111.4	171.4
	282.9	282.9	102.9	282.9	12.9	102.9	192.9	282.9	342.9	42.9	102.9	162.9	222.9
	334.3	334.3	154.3	334.3	64.3	154.3	244.3	334.3	34.3	94.3	154.3	214.3	274.3

- in the shifted centre line (SCL), which has a 5 mm offset relative to the CL;
- in the mid triangle line (MTL), which is between the CL and the next CCO line, in the positive direction along z axis. For WP/α combinations where this length exceeds $L/2$ or is close to the edge, coordinate $z = L/4$ is adopted.

The configurations that applied this exception rule for defining the MTL location were $WP = 0$ (all values of α), $WP = 1$ ($\alpha = 15°, 25°, 35°, 45°, 55°$), $WP = 3$ ($\alpha = 15°, 25°$), and $WP = 5$ ($\alpha = 15°$).

3. Results and discussions

In this section, the stress profiles and stiffness values for every *WP* analysed are presented, also focusing on the effects of angle and number of layers. Four winding patterns (plus the baseline cylinder disregarding the *WP*), four different numbers of layers, and six winding angles are considered in this analysis. Furthermore, the cylinders are subjected to three different loading conditions and their respective boundary conditions. A total number of 360 simulations is performed. The available data for supporting the statements are provided in the *supplementary material* for verification, repeatability, and further usage.

3.1. Axial compression

This analysis shows stress oscillations around the interweaving regions, following observations from experimental data [25]. Fig. 6 plots the stress σ_1 (see Fig. 3 for the local coordinate system) over the cylinder, highlighting the points with the highest stress concentration,

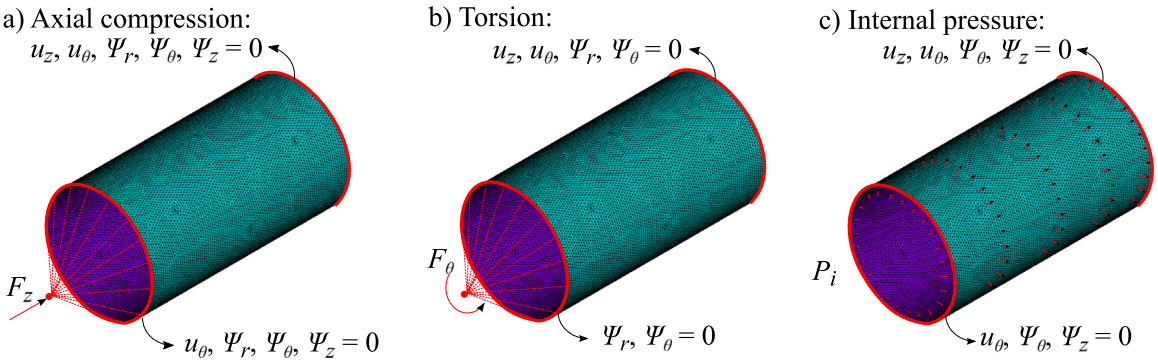

Fig. 5. Loads and boundary conditions on the cylinders under (a) axial compression (b) torsion, and (c) internal pressure loads.

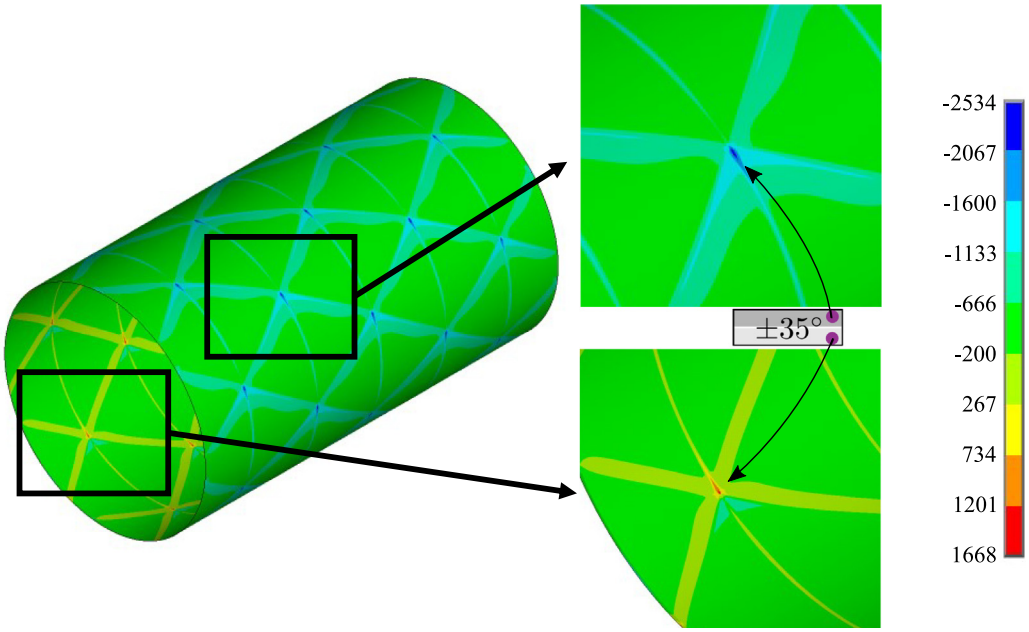

Fig. 6. Stress σ_1 of a cylinder subjected to axial compression highlighting the stress concentrations in the interweaving (CCO and HCO) regions. Parameters used: $N = 1$; $\alpha = 35°$; and WP=7.

which is in the transition between two diamond shapes along a CCO line. Here, it is important to notice that these concentrations might appear due to the sudden shift in the material properties given the modelling procedures herein adopted. Still, the interweaving generates some concentrations as shown numerically in [28,29] and experimentally in [25]. In Fig. 6, stress plots incorporate a laminate scheme of the analysed geometry, with a solid dot pointing to the through-thickness coordinate where the stress is evaluated in the respective plot.

The stresses in σ_1, σ_2, and τ_{12} are plotted for different WPs in Fig. 7. The WP=5 was omitted from this figure to allow better visualization, but it can be found in the Supplementary Material. For the stress fields σ_1 and σ_2, the stress peaks in the CL region are higher, and the number of peaks equals the WP number since this is also the number of diamond shape transitions along this line. Regarding the SCL region, due to the small offset applied, peaks are observed in the same locations as in CL, but with smaller amplitude. Also, when measured far from the interweaving regions, in the RL region, the developed stress field is very similar to the stress developed in the model without pattern consideration ($WP = 0$). In other words, the stresses are similar to a regular laminate away from the interweaving region. On the MTL, the distance between two interweaving regions along the circumferential direction is maximized. Therefore, the peaks when crossing them are clearly distinguished in Fig. 7, yielding a total of $2 \times WP$ peaks.

Differently from σ_1 and σ_2, τ_{12} maintains the magnitude but changes sign when switching from $-\alpha$ to $+\alpha$ and the other way around. This change can be observed in the MTL region in Fig. 7, showing a small tip before stabilizing. The peak increases as the WP increases. The SCL region quickly crosses the $+\alpha$ ply, forming a peak in the plots.

On a second analysis, $WP = 5$ and N is varied. The results are depicted in Fig. 8. The stress oscillations when approaching the interweaving regions are significantly smoothed through the addition of more layers. In the MTL region, for example, while the single-layer configuration yielded σ_1 stresses between approximately −650 MPa and 0 MPa, with $N = 6$ the oscillations are narrowed and kept within the range of −560 MPa and −530 MPa. Results for σ_2 follow the same behaviour, despite the lower absolute stress values, significantly reducing stress concentrations as more layers are added to the laminate. As for τ_{12}, no oscillations are observed, but the peaks that occur when shifting

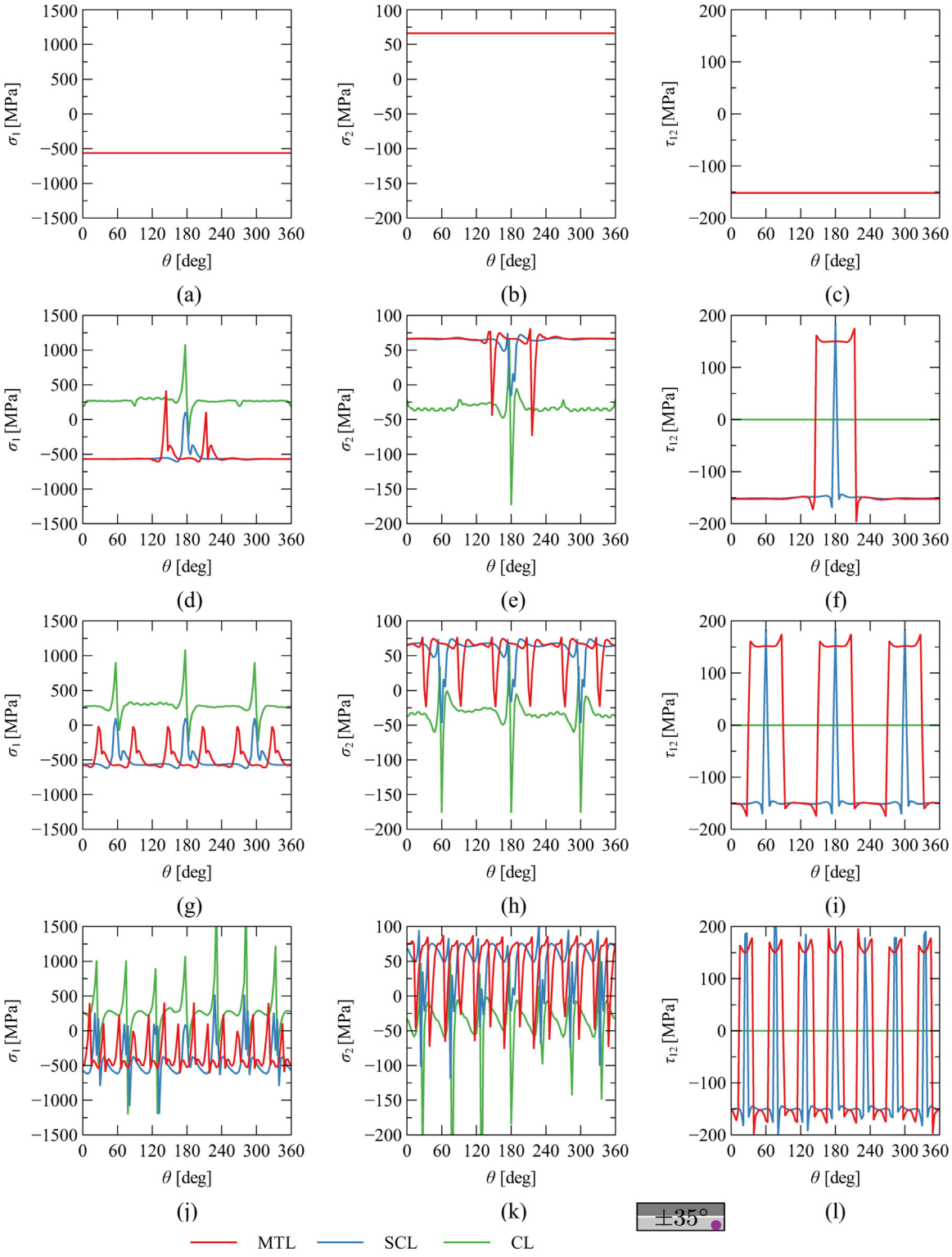

Fig. 7. Stress variation in the bottom layer along the circumferential direction at CL, SCL, and MTL regions in a cylinder under axial compression. Parameters used: $N = 1$ and $\alpha = 35°$; columns define the stress: 1st - σ_1, 2nd - σ_2, and 3rd - τ_{12}; lines represent the WP: 1st - $WP = 0$, 2nd - $WP = 1$, 3rd - $WP = 3$, and 4th - $WP = 7$.

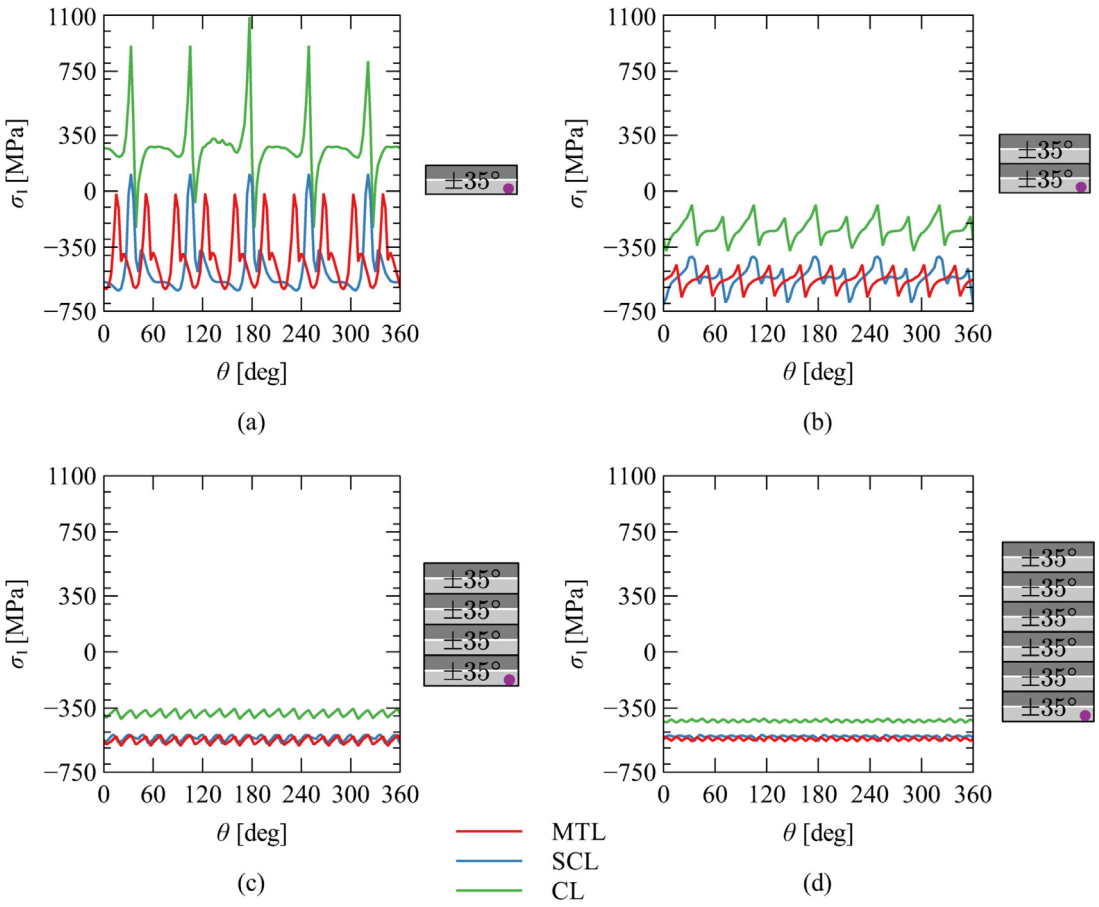

Fig. 8. Stress σ_1 at the bottommost layer along the CL, SCL, and MTL regions in a cylinder under axial compression. Parameters used: $WP = 5$; $\alpha = 35°$; and (a) $N = 1$, (b) $N = 2$, (c) $N = 4$, (d) $N = 6$.

between plies (i.e., when crossing the HCO region), depicted in Fig. 7 for $N = 1$, are also mitigated with the addition of more layers, and the stresses along the MTL region assumes a square wave shape.

When varying both *WP* and *N*, shear stresses close to zero are seen in the CL region and also in all CCO lines. An explanation for this is illustrated in Fig. 9, where τ_{12} values measured at nodes and elements are depicted in a colour scale, considering a cylinder with $N = 6$ to mitigate stress concentrations. As can be seen, the stress measurements at the elements do not capture this null shear stress, and the elements adjacent to the CL region yield values close to the ones measured in the MTL region. However, when extrapolating the stresses in these elements to nodes that fall exactly in the CL region, the nodal approach smooths the $+\tau_{12}$ stress in the $-\alpha$ ply with the $-\tau_{12}$ stress in the $+\alpha$ ply, yielding a null stress. For this reason, stress measurements along the CL region are avoided.

A closer analysis of the stress levels at the MTL region reveals a discrepancy in the values at different points along the thickness. As can be seen in Fig. 10, for $N = 1$ the stress in the bottom-most ($-\alpha$) and topmost ($+\alpha$) oscillated around different values, but this difference falls strongly for $N = 6$. The stress distribution for $N = 6$ (Fig. 10(b)) suggests an influence of bending stresses, which is expected for non-symmetric laminates, even under pure axial stress conditions. Corroborating with former works, the addition of more layers decreased the *WP* effect [10].

These results also show that the layers experience peaks in the same angular positions along the circumferential direction. For instance, a stress concentration in the interweaving region of the bottom-most layer led to stress concentrations in all the other layers, even the topmost, yielding the smoothing effect observed in Figs. 8 and 10. Nonetheless, this effect occurs because it is necessary to avoid the transitions between $-\alpha$ and $+\alpha$ plies in the same angular positions. In the above examples, where they occurred always in different locations, the total number of peaks is equal to $N \times WP$. However, as reported in Table 2, this is not the case for the construction with $WP = 3$ and $N = 6$. In this case, the diamond-shaped structures are constructed exactly one over another, yielding a stress distribution similar to the expected for $N = 3$. In this specific case, the configuration with $N = 4$ produces fewer stress concentrations than the configuration with $N = 6$ (see Fig. 11).

3.2. Torsion

Regarding the torsional behaviour, stress fields for a particular case ($WP = 5$, $\alpha = 55°$, and $N = 6$) can be viewed in Fig. 12. As for in the case of axial compression loading condition, transitioning regions between plies are the main source of stress concentrations, but now the stresses σ_1 and σ_2 reach zero values in the CL region and change their sign when crossing the interweaving regions. In comparison to Fig. 6, the stress concentration region around the CCO lines is wider.

Stresses for different winding angles are plotted in Fig. 13. As expected, a shear value close to zero is obtained for $\alpha = 45°$. This plot also shows how the stress oscillations presented in τ_{12} under torsion are analogous to the ones in σ_1 and σ_2 under compression, while the stresses σ_1 and σ_2 under torsion are analogous to the stress τ_{12} under compression (see Fig. 7).

As observed in Fig. 14 and similarly to the observations made for the cylinders in axial compression, the stress peaks are also reduced when more than one double layer is considered. The oscillations when abruptly changing the sign of σ_1 were also smoothed. Since in this case a greater α value was considered (65°), even the SCL region could

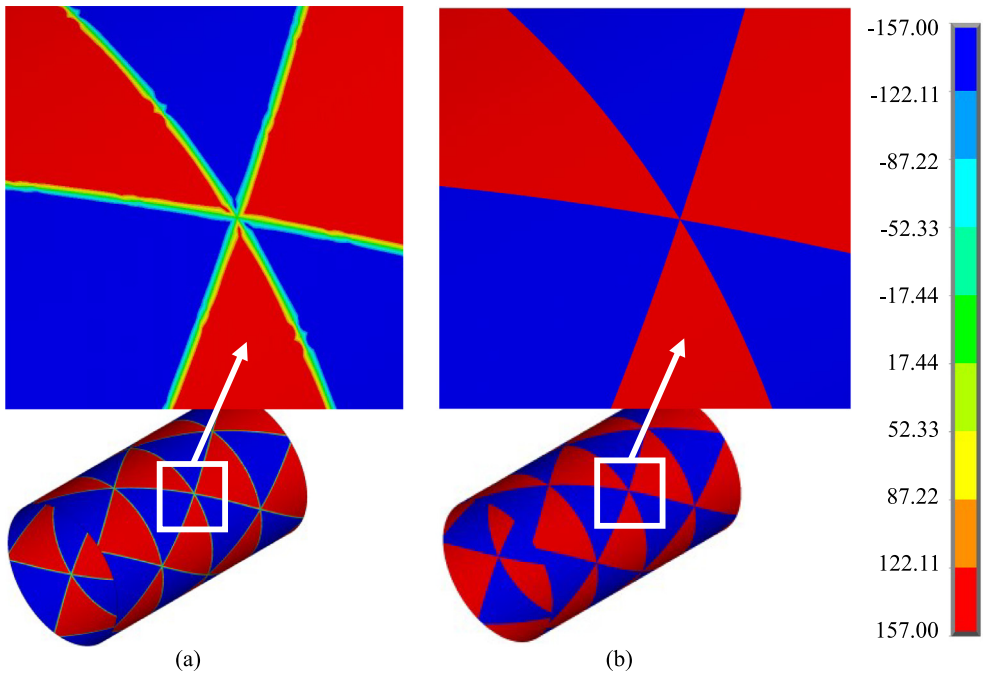

Fig. 9. The τ_{12} stress computation (a) extrapolated to the nodes and (b) using the interpolation functions in the elements. Parameters used: $WP = 5$; $\alpha = 35°$; and $N = 6$.

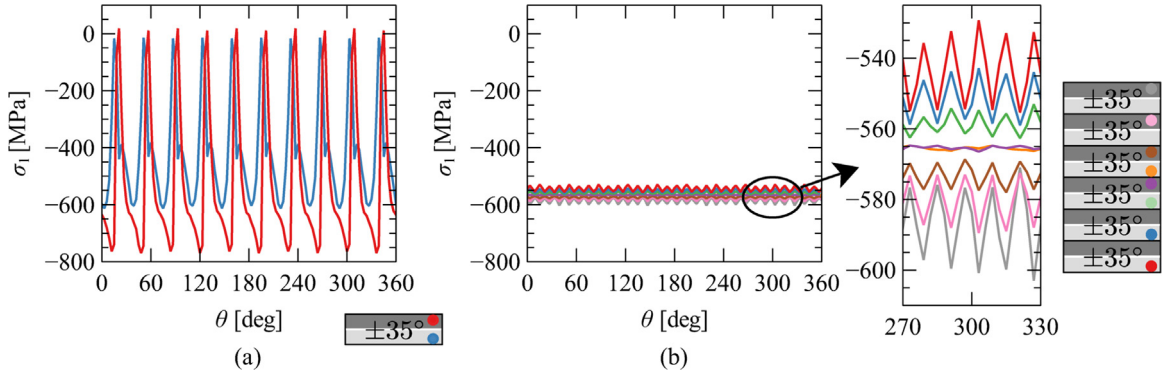

Fig. 10. The σ_1 stress along the MTL region for different plies. Parameters used: $WP = 5$; $\alpha = 35°$; and (a) $N = 1$, (b) $N = 6$.

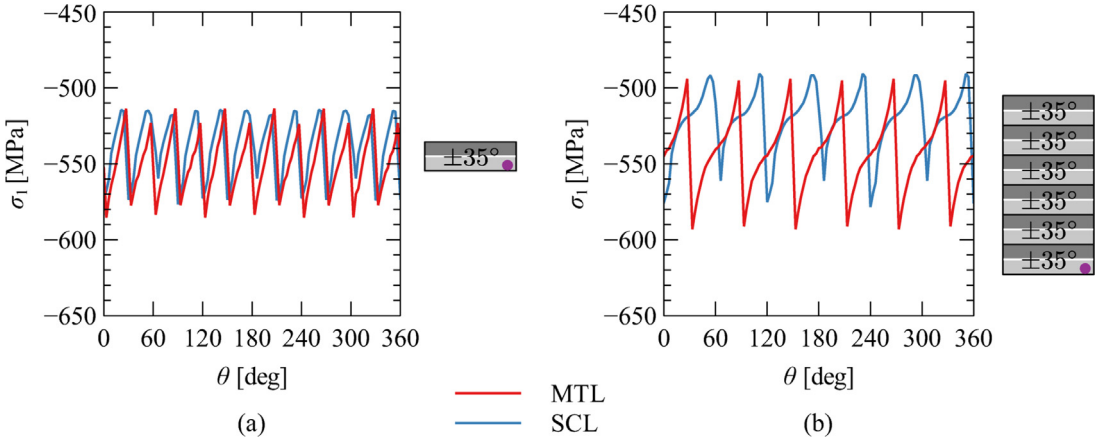

Fig. 11. The σ_1 stress along the MTL and SCL regions at the bottom layer. Parameters used: $WP = 3$; $\alpha = 35°$; and (a) $N = 4$, (b) $N = 6$.

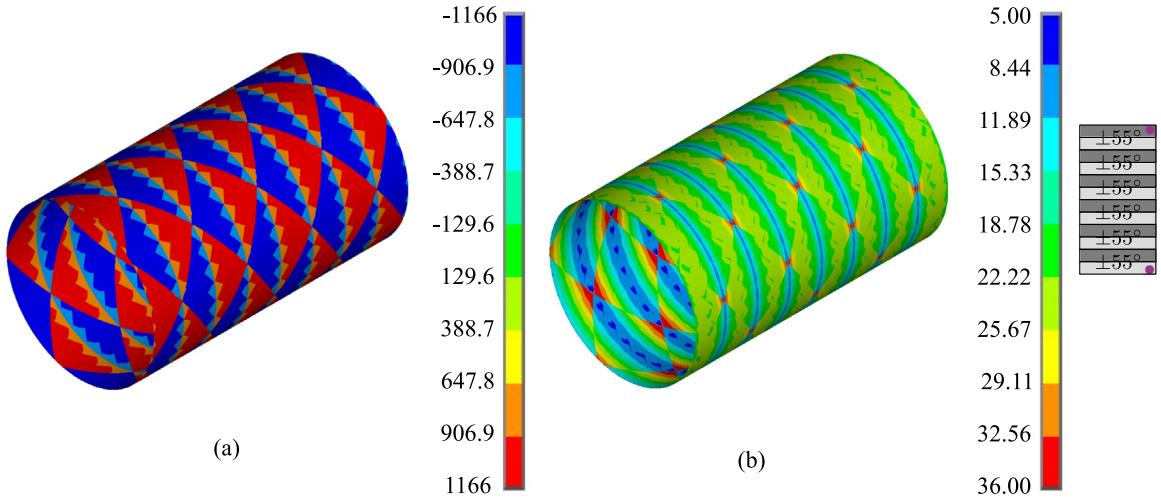

Fig. 12. The (a) σ_1 and (b) τ_{12} stress fields in the bottom and top layers of a cylinder subjected to torsion. Parameters used: $WP = 5$; $\alpha = 55°$; and $N = 6$.

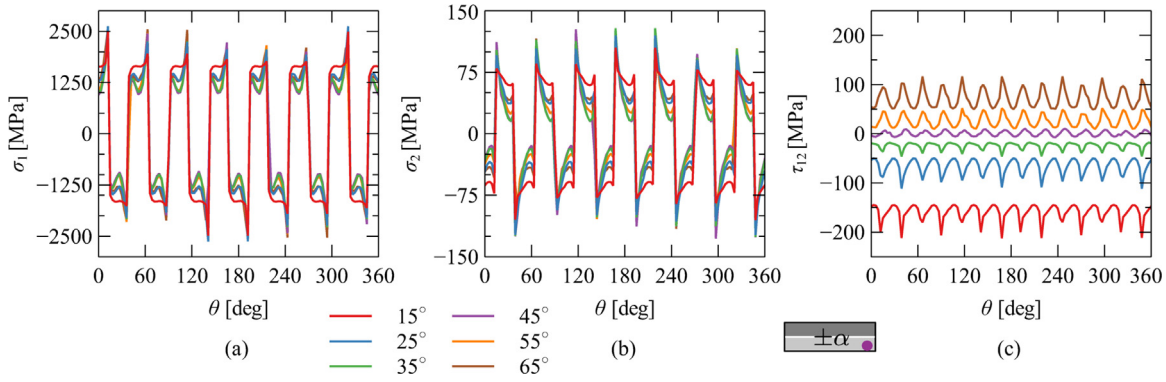

Fig. 13. The (a) σ_1, (b) σ_2, and (c) τ_{12} stress fields for a cylinder in torsion evaluated along the MTL region for different winding angles. Parameters used: $WP = 7$ and $N = 1$.

capture two distinguish peaks for every *WP* (see Fig. 14(b)). It is also possible to notice that, differently from axial compression, the SCL region does not reach the stress value from the MTL region due to the wider stress concentration region around the CCO region.

3.3. Internal pressure

Cylinders under internal pressure show stress concentrations in similar areas as seen for the other two loading cases previously results, as depicted in Fig. 15, where the hoop stress σ_θ was included along with the other three local stresses. The shear stress changes abruptly when crossing the interweaving regions, reaching a null value in the CCO lines due to the nodal extrapolation. Fig. 16 shows that stress peaks are also observed when crossing interweaving regions for σ_θ and that these peaks could also be significantly reduced by increasing the number of layers. A qualitative behaviour analogous to axial compression for the three stresses in local coordinates is observed along the circumferential direction.

Aiming to simulate a more complex structural model under internal pressure and verify with arbitrary parameters if the stress behaviour remains the same, one considers different *WP*, ϕ, and α for each layer. The inputs are given in Table 3. Results are reported in Fig. 17 for two coordinates along z, 24.37 mm and 73.11 mm. These positions were selected as they are distant from any CCO lines generated by the *WP* of the set. Stress concentrations are lower than the single-layer

Table 3
Input parameters for a filament wound cylinder with four layers.

Layer	*WP*	α(°)	ϕ(°)
1	3	56	0
2	6	16	42
3	2	43	11
4	4	38	72

configurations, but they could not decrease in the same proportion as in the case with regular layers, which is expected considering that in this case, stress concentrations have the likelihood of falling in similar angular positions, resulting in stress superpositions. In addition, due to the transferring of stress concentrations observed in Section 3.1, there is a large difference in the relative stress concentrations among layers. In the bottom layer, where the hoop stress is higher in view of the higher α, the maximum deviation of the stresses relative to the reference configuration is 9%. In the top layer this angle is lower, and so is the stress, but the maximum deviation increases to 27%.

3.4. Stiffness

The stiffness is herein defined as the ratio between the applied force and the generated displacement, measured in the same direction as the loading. By using $WP = 0$ as a reference, one can also quantify the

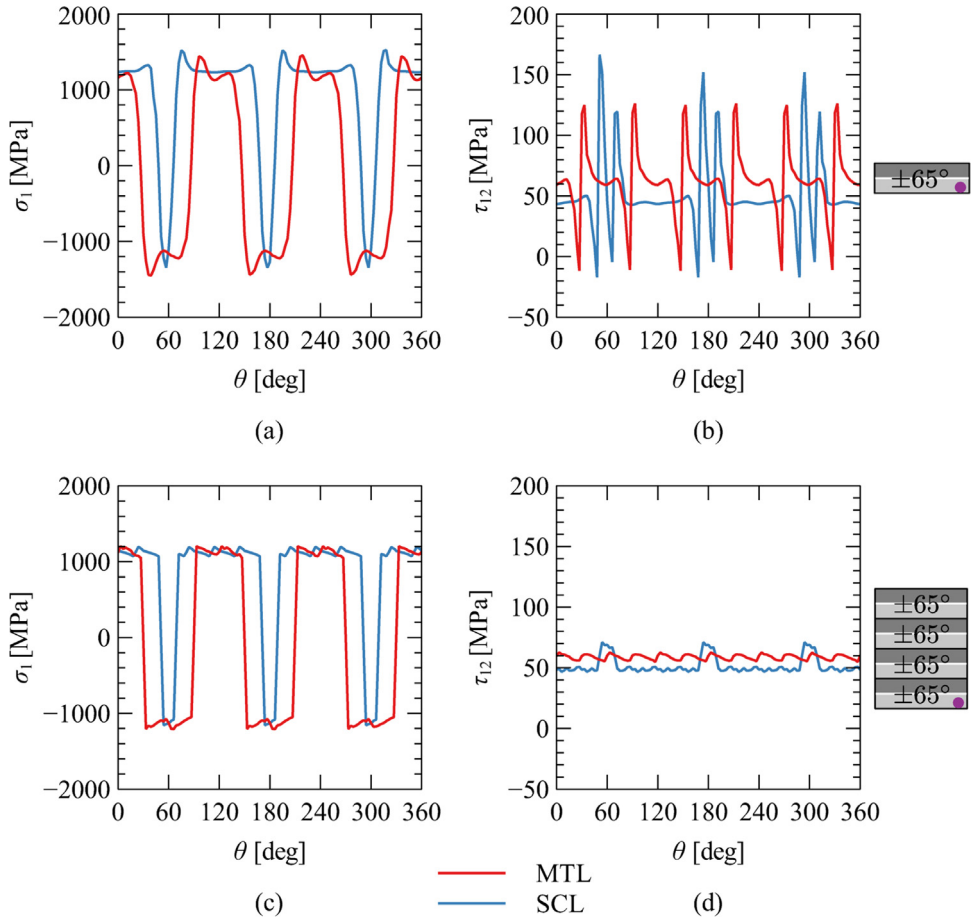

Fig. 14. The (a) σ_1 and (b) τ_{12} stress fields with $N = 1$, (c) σ_1 and (d) τ_{12} stresses, with $N = 4$, in the bottom layer of a cylinder subjected to torsion. Parameters used: $WP = 3$ and $\alpha = 65°$.

effect of neglecting the *WP* in the numerical models. A comparison between deformed shapes under axial compression and torsion is shown in Figs. 18 and 19. For both loading conditions, with N=6, the interweaving path (both HCO and CCO regions) becomes indistinguishable, even with a magnification factor of 5.

Results for cylinders in axial compression are shown in Fig. 20, where the deviations are computed from the reference configuration (*WP*=0). Deviations up to −7.4% are observed for the configuration with one layer, while for the two layers configuration, the values are below 1%. In the cases with four and six layers, differences are negligible. Deviations reach their highest value for $\alpha = 25°$, decreasing as α increases. This can be explained by analysing the stress fields along the MTL region for different values of α, plotted in Fig. 21. The configuration with $N = 1$ and $WP = 7$ is chosen since this set yields the highest stiffness deviations. As can be seen, stress concentrations are higher in σ_1, so it is expected the stiffness deviation to be lower in the configurations where σ_2 plays the major role ($\alpha = 55°, 65°$). While the values of σ_1 are very similar for 15°, 25°, and 35°, the configuration with $\alpha = 25°$ shows the highest concentration level in the interweaving region relative to τ_{12}. This concentration lowers the stiffness and this configuration presents the highest deviation.

Regarding the influence of the *WP* on the axial stiffness, Fig. 20 shows an increasing deviation as the *WP* increases, with an approximately linear correlation for the configuration with $N = 1$. For the other ones, the variation was smaller, and numerical deviations can easily mitigate the pattern influence. Fig. 4(a) reveals a similar trend in the size of the HCO region when going from *WP*=1 to *WP*=7, indicating a relation between stiffness deviations and the length of this interweaving region. This observation was verified by taking the configuration with the highest deviation ($\alpha = 25°$), and extrapolating it to a model with *WP*=15 and $N = 1$, which resulted in a deviation of −15.81%. The addition of this value in the plot from Fig. 20(b) and subsequent fitting, considering a linear tendency, yields a coefficient of determination of 0.9998.

Results for torsional load conditions are shown in Fig. 22. Differently than for the axial compression results, no linear behaviour is observed for the deviation as a function of the *WP*. This could be explained by examining Fig. 19, where deformations are observed along the CCO lines, while in Fig. 18 they are invisible in that region. The number of CCO lines also increases as the *WP* increases but in a non-proportional fashion. As illustrated in Fig. 4, for instance, the number of CCO lines are 1, 3, 3, and 5, for *WPs* 1, 3, 5, and 7, respectively. The lowest decrement in stiffness deviation observed in Fig. 22(c) occurs between *WPs* 3 and 5, where the number of CCO lines did not change. This observation holds also for all the other angles analysed, indicating a strong link between the torsion stiffness and the number of CCO lines. Therefore, while the axial stiffness is sensible to the size of the HCO region, the torsion stiffness depends on the size of both the HCO and CCO regions.

Regarding the influence of α on the torsional stiffness, more significant deviations are computed relative to the axial stiffness. They are present in the entire α range for the one-layer configuration, reaching

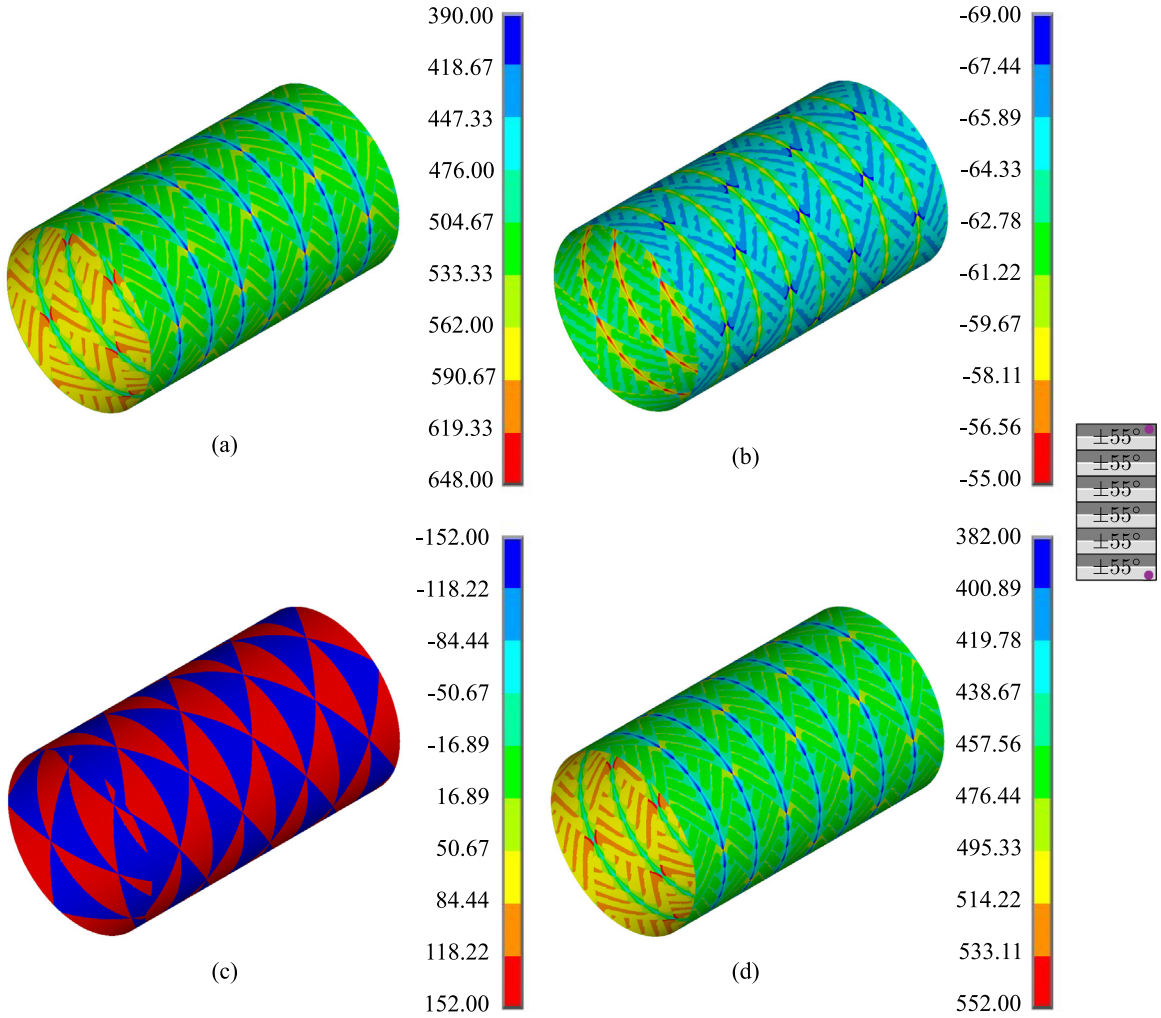

Fig. 15. The (a) σ_1, (b) σ_2, (c) τ_{12}, and (d) σ_θ stress fields in the bottom and top layers of a cylinder subjected to internal pressure. Parameters used: $WP = 5$; $\alpha = 55°$; and $N = 6$.

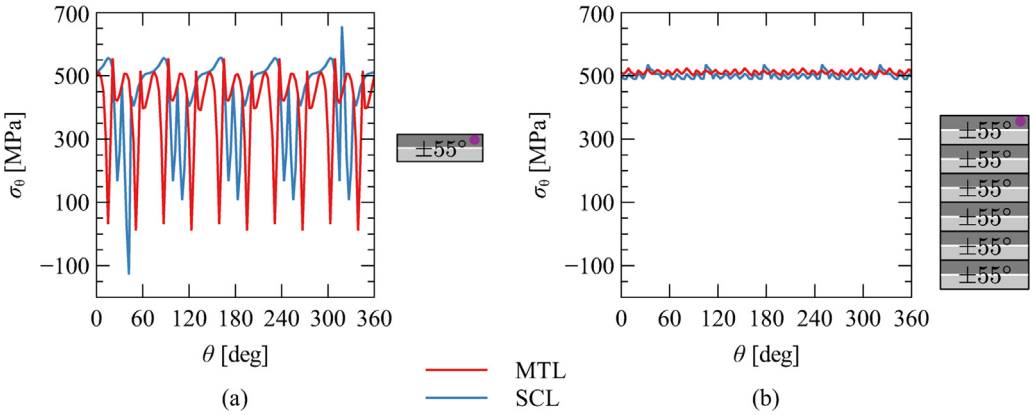

Fig. 16. Comparison of σ_θ at MTL and SCL areas with (a) $N = 1$ and (b) $N = 6$, subjected to internal pressure. Parameters used: $WP = 5$ and $\alpha = 55°$.

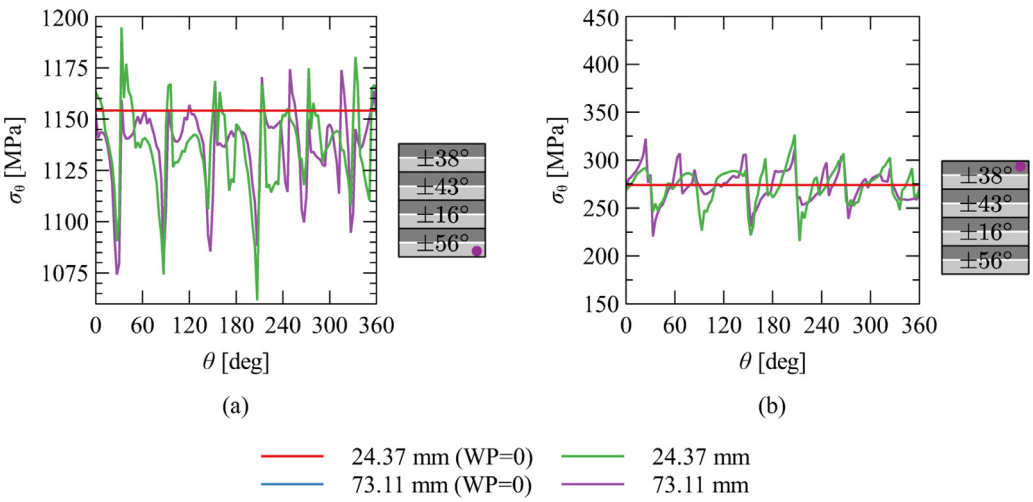

Fig. 17. The stress σ_θ along the (a) bottom and (b) top plies for a cylinder with WP, α, and ϕ arbitrarily defined.

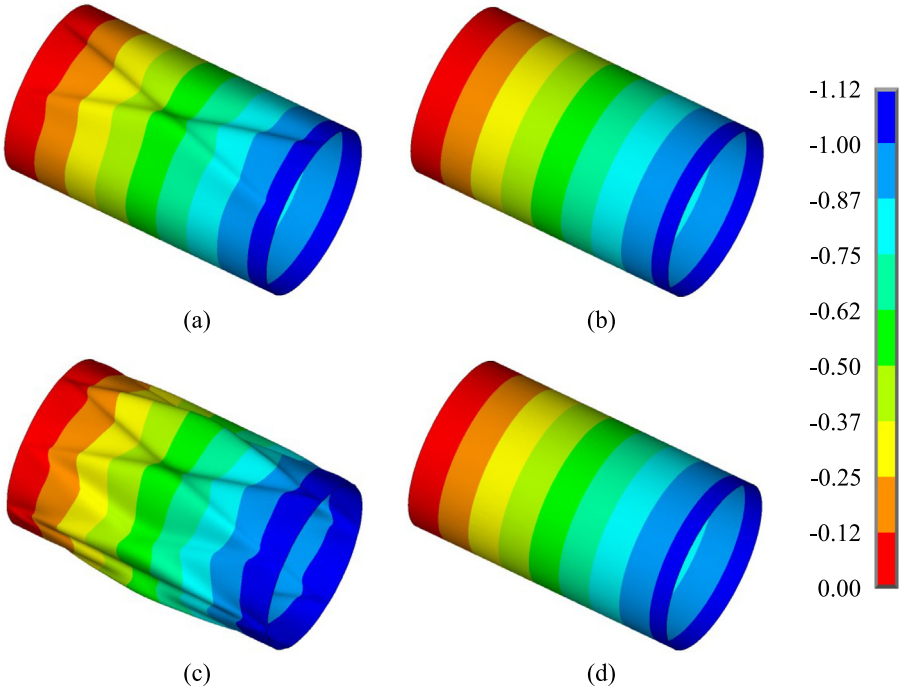

Fig. 18. Displacement u_z [mm] in the deformed shape with a 5× magnification factor for a cylinder under axial compression with $\alpha = 15°$ and: (a) $N = 1$ and $WP = 1$, (b) $N = 6$ and $WP = 1$, (c) $N = 1$ and $WP = 7$, (d) $N = 6$ and $WP = 7$.

the value of 25.2% in the worst case, while with two layers the deviations keep between 2.3% and 4.8%. In conjunction with the axial stiffness, four and six layers yield negligible deviations. As can be seen in Fig. 13, the stress peaks, observed in τ_{12} for axial compression load when crossing the CL region, can now be observed for σ_1 and σ_2. As for the compression load condition, their magnitudes correlate with the deviations presented in Fig. 22, yielding deviations proportional to these peaks.

The interweaving regions are modelled as straight lines and the effective material properties change abruptly from one to another. This unavoidable simplification might generate a higher stress concentration, which means that the values found might be slightly higher than reality. Support from experimental data would be a welcome addition to account for possible corrections of stiffness for double layers with $N \leq 4$.

4. Conclusions

This work proposed a numerical methodology to evaluate the winding pattern effects on composite cylinders under axial compression, torsion, and internal pressure loading cases. The influence of the winding angle and several layers were also considered. The following conclusions can be drawn:

- Stress concentrations are observed in the interweaving regions in all tested load conditions. Under axial compression, the HCO regions are wider and CCO are thinner, in comparison to torsion. Away from these regions, the stress value of a regular laminate composite is observed. Despite increasing the number of stress concentrations, no evidence that the WP increases the magnitude of these stresses was found;
- Stress concentrations of one layer propagate to all the others, but their magnitude is considerably reduced by adding layers.

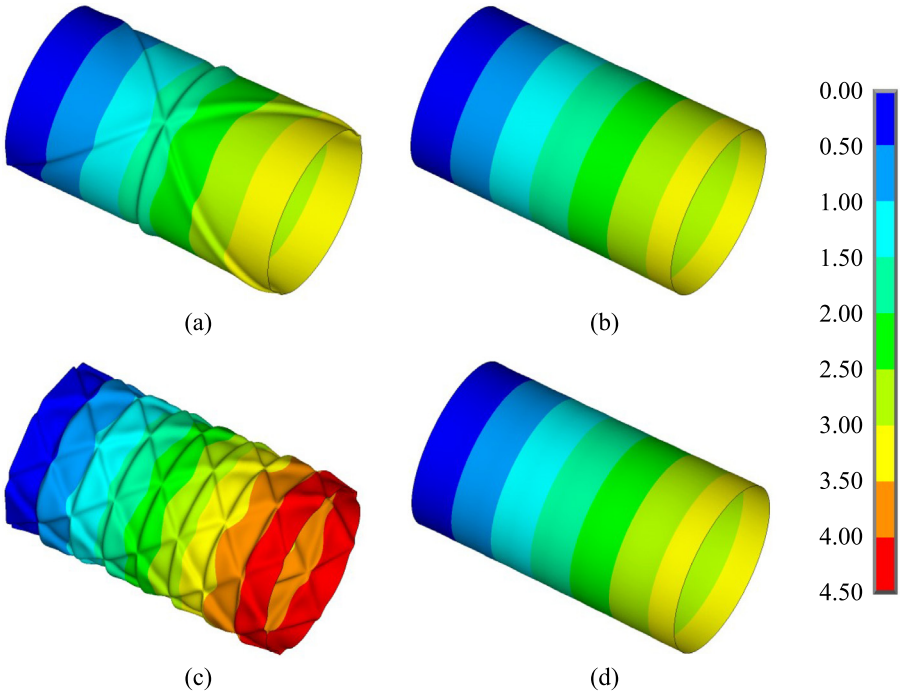

Fig. 19. Displacement u_θ [mm] in the deformed shape with a 5× magnification factor for a cylinder under torsion with $\alpha = 45°$ and: (a) $N = 1$ and $WP = 1$, (b) $N = 6$ and $WP = 1$, (c) $N = 1$ and $WP = 7$, (d) $N = 6$ and $WP = 7$.

Nonetheless, when a stress concentration of one layer falls in the same angular position as another layer of the cylinder a superposition effect takes place, and its magnitude increases;

- Axial stiffness is very sensitive to the size of the HCO region and inversely proportional to it, but the *WPs* influence is negligible for cylinders with more than 2 layers;
- Regarding torsion stiffness, it is very sensitive to the size of the CCO region and inversely proportional as well. Nevertheless, *WPs* influence is negligible for cylinders with more than 4 layers;
- The influence of *WP* in stress concentrations and both axial and torsion stiffness varies according to the winding angle.

Besides the methodology proposed in the present study, which can be applied to many similar cases, the stress results obtained show a systematic behaviour that helps to clarify some aspects of the mechanical behaviour of FW cylinders. In particular, it was shown that pathological stress concentration distributions manifest along distinct regions intrinsic to the FW process. Their effects were numerically mapped for various combinations of patterns and winding angles, and the mitigation of these effects, as the number of layers increased, became clear. These findings, along with the mapping of the axial, torsional, and pressure stiffness computed in the present work, represent a valuable asset for Engineering analysis of these components, since these aspects can now be incorporated into their design and contribute significantly to better safety levels, as well as an overall understanding of their response. Experimental tests, assisted by digital image correlation, are the next step of this study to determine the source and location of stress concentrations herein observed and to validate the numerical findings presented here.

CRediT authorship contribution statement

Eduardo A.W. de Menezes: Writing – original draft, Validation, Software, Methodology, Investigation, Formal analysis. **Tales V. Lisbôa:** Writing – original draft, Software, Methodology, Investigation, Formal analysis, Data curation, Conceptualization. **José Humberto S. Almeida Jr.:** Writing – original draft, Visualization, Methodology, Validation, Investigation, Formal analysis, Conceptualization. **Axel Spickenheuer:** Funding acquisition. **Sandro C. Amico:** Visualization, Resources, Project administration. **Rogério J. Marczak:** Writing – review & editing, Supervision, Formal analysis.

Declaration of competing interest

The authors disclose to have no financial and personal relationships with other people or organizations that could inappropriately influence their work.

Data availability

Data will be made available on request.

Acknowledgements

The authors are grateful to CAPES/DAAD (PROBRAL project 88881.198774/2018-01) and FAPERGS, Brazil (Inova Clusters Tecnológicos n. 22/2551-0000839-9) for their financial support. HA is supported by the Royal Academy of Engineering, United Kingdom under the Research Fellowship scheme [Grant No. RF/201920/19/150]. RJM is supported by CNPq under the grant [317140/2021-3].

Appendix A. Supplementary data

Supplementary material related to this article can be found online at https://doi.org/10.1016/j.tws.2023.111041. The raw data and additional plots to supplement the results herein presented can be found in the uploaded supplementary spreadsheet.

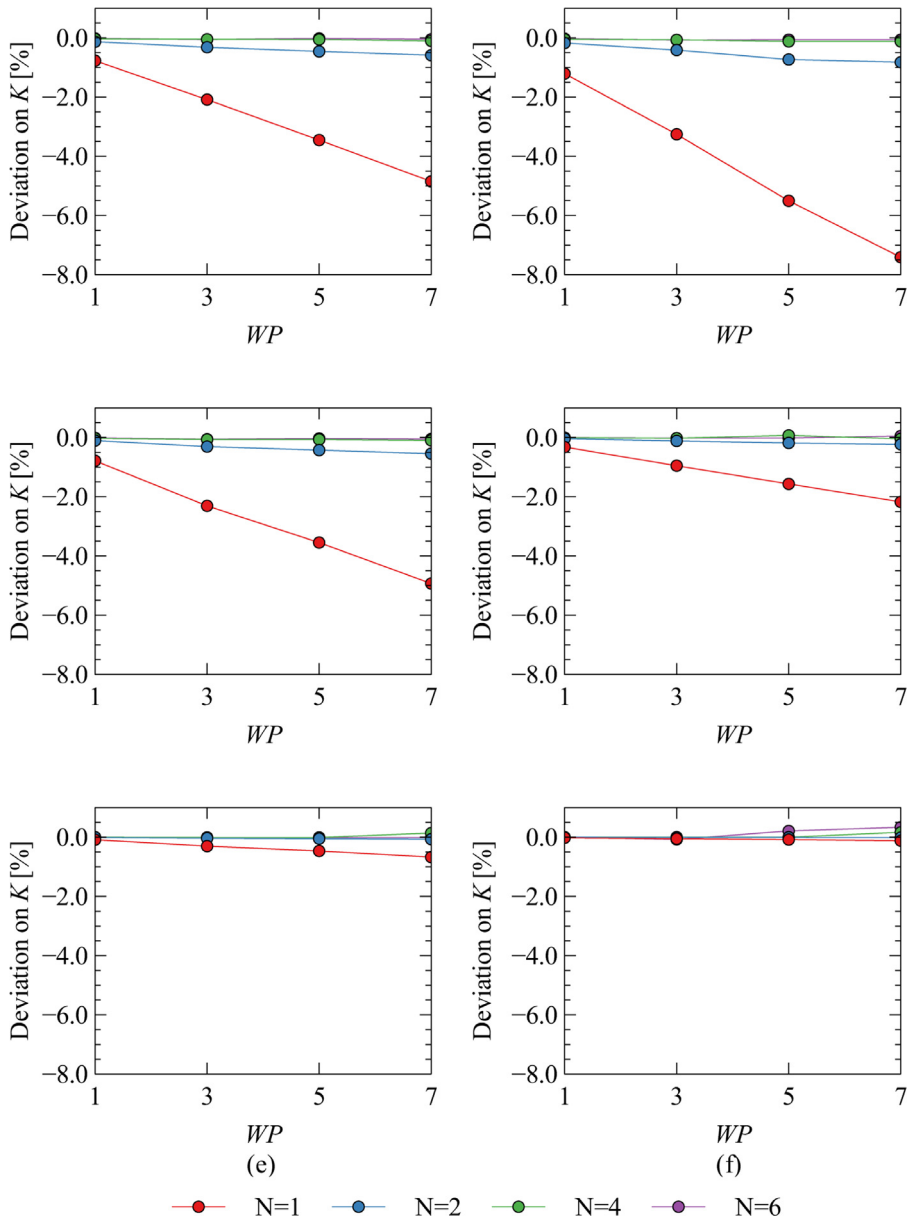

Fig. 20. Deviation relative to the reference configuration ($WP = 0$) on the axial stiffness as a function of WP in a cylinder under compression loading. The analysed winding angles are (a) 15°, (b) 25°, (c) 35°, (d) 45°, (e) 55°, and (f) 65°.

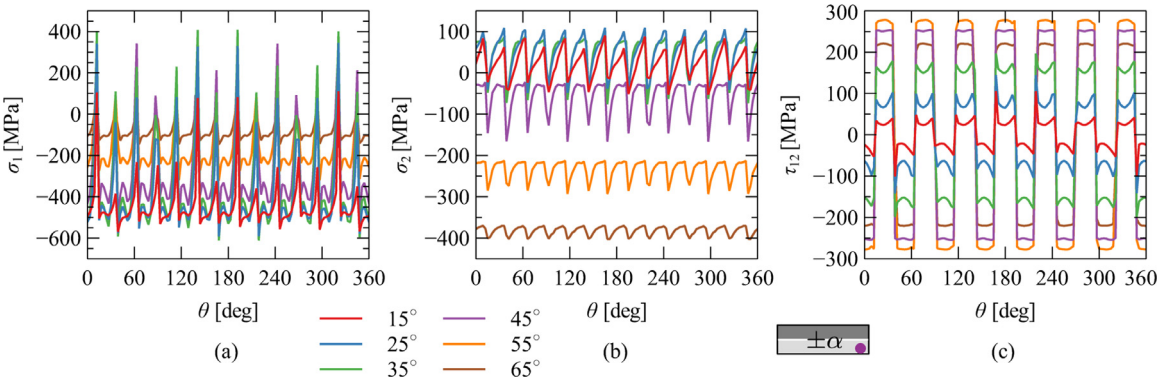

Fig. 21. (a) Stresses σ_1, (b) σ_2, and (c) τ_{12} stresses along the MTL region for a cylinder in axial compression for different winding angles. Parameters used: $WP = 7$; and $N = 1$.

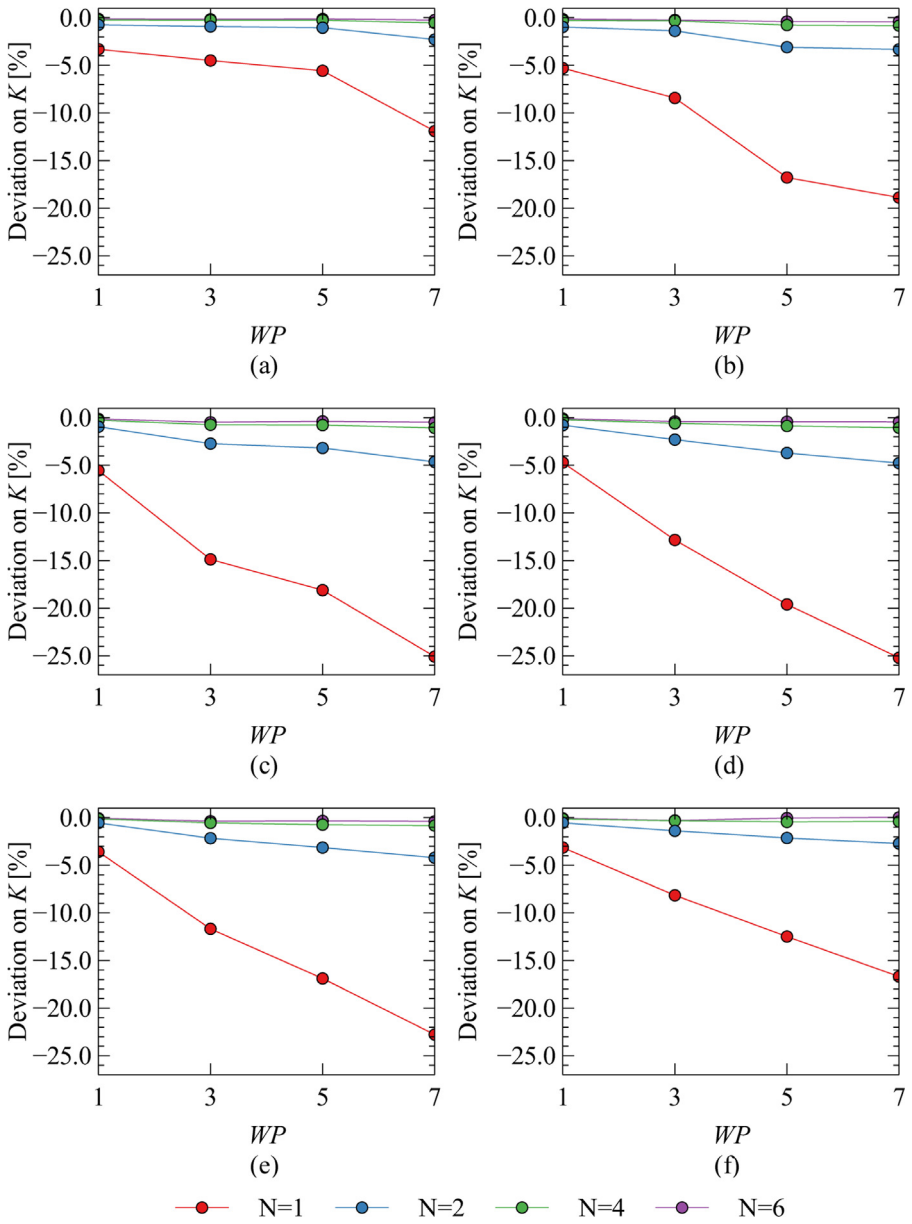

Fig. 22. Deviation relative to the reference configuration (*WP* = 0) on the torsion stiffness as a function of *WP* in wound cylinders under torsion loading. The analysed winding angles are (a) 15°, (b) 25°, (c) 35°, (d) 45°, (e) 55°, and (f) 65°.

References

[1] M. Sayem Uddin, E.V. Morozov, K. Shankar, The effect of filament winding mosaic pattern on the stress state of filament wound composite flywheel disk, Compos. Struct. 107 (1) (2014) 260–275, http://dx.doi.org/10.1016/j.compstruct.2013.07.004.

[2] I.H. Dalibor, T.V. Lisbôa, R.J. Marczak, S.C. Amico, A geometric approach for filament winding pattern generation and study of the influence of the slippage coefficient, J. Braz. Soc. Mech. Sci. Eng. 41 (12) (2019) 1–16, http://dx.doi.org/10.1007/s40430-019-2083-2.

[3] C.J. Moon, I.H. Kim, B.H. Choi, J.H. Kweon, J.H. Choi, Buckling of filament-wound composite cylinders subjected to hydrostatic pressure for underwater vehicle applications, Compos. Struct. 92 (9) (2010) 2241–2251, http://dx.doi.org/10.1016/j.compstruct.2009.08.005.

[4] P. Stedile Filho, J.H.S. Almeida Jr., S.C. Amico, Carbon/epoxy filament wound composite drive shafts under torsion and compression, J. Compos. Mater. 52 (8) (2018) 1103–1111, http://dx.doi.org/10.1177/0021998317722043.

[5] F. Eggers, J.H.S. Almeida Jr., C.B. Azevedo, S.C. Amico, Mechanical response of filament wound composite rings under tension and compression, Polym. Test. 78 (January) (2019) 105951, http://dx.doi.org/10.1016/j.polymertesting.2019.105951.

[6] Z. Sun, J. Xiao, X. Yu, R. Tusiime, H. Gao, W. Min, L. Tao, L. Qi, H. Zhang, M. Yu, Vibration characteristics of carbon-fiber reinforced composite drive shafts fabricated using filament winding technology, Compos. Struct. 241 (2020) 111725, http://dx.doi.org/10.1016/j.compstruct.2019.111725.

[7] M.B. Antunes, J.H.S. Almeida Jr., S.C. Amico, Curing and seawater aging effects on mechanical and physical properties of glass/epoxy filament wound cylinders, Compos. Commun. 22 (2020) 100517, http://dx.doi.org/10.1016/j.coco.2020.100517.

[8] K.-C. Shen, G. Pan, Buckling and strain response of filament winding composite cylindrical shell subjected to hydrostatic pressure: Numerical solution and experiment, Compos. Struct. 276 (2021) 114534, http://dx.doi.org/10.1016/j.compstruct.2021.114534.

[9] J.H.S. Almeida, L. St-Pierre, Z. Wang, M.L. Ribeiro, V. Tita, S.C. Amico, S.G. Castro, Design, modeling, optimization, manufacturing and testing of variable-angle filament-wound cylinders, Composites B 225 (2021) 109224, http://dx.doi.org/10.1016/j.compositesb.2021.109224.

[10] E.V. Morozov, The effect of filament-winding mosaic patterns on the strength of thin-walled composite shells, Compos. Struct. 76 (1–2) (2006) 123–129, http://dx.doi.org/10.1016/j.compstruct.2006.06.018.

[11] C.B. Azevedo, J.H.S. Almeida Jr., H.F. Flores, F. Eggers, S.C. Amico, Influence of mosaic pattern on hygrothermally-aged filament wound composite cylinders under axial compression, J. Compos. Mater. 54 (19) (2020) 2651–2659, http://dx.doi.org/10.1177/0021998319899144.

[12] J.H.S. Almeida Jr., T.V. Lisbôa, A. Spickenheuer, L. St-Pierre, A sequential finite element model updating routine to identify creep parameters for filament wound

composite cylinders in aggressive environments, Comput. Struct. 276 (2023) 106939, http://dx.doi.org/10.1016/j.compstruc.2022.106939.

[13] T.V. Lisbôa, J.H.S. Almeida Jr., I.H. Dalibor, A. Spickenheuer, R.J. Marczak, S.C. Amico, The role of winding pattern on filament wound composite cylinders under radial compression, Polym. Compos. 41 (6) (2020) 2446–2454, http://dx.doi.org/10.1002/pc.25548.

[14] S.J. Claus, Effects of winding pattern on the compressive behavior of filament-wound cylinders, in: Proceedings of the 7th Technical Conference of the American Society for Composites, 1992, pp. 258–265.

[15] H.T. Hahn, D.W. Jensen, S.J. Claus, S.P. Pai, P.A. Hipp, Structural design criteria for filament-wound composite shells, NASA CR 195125 (1994) 1–172.

[16] J. Rousseau, D. Perreux, N. Verdière, The influence of winding patterns on the damage behaviour of filament-wound pipes, Compos. Sci. Technol. 59 (9) (1999) 1439–1449, http://dx.doi.org/10.1016/S0266-3538(98)00184-5.

[17] H. Hernández-Moreno, B. Douchin, F. Collombet, D. Choqueuse, P. Davies, Influence of winding pattern on the mechanical behavior of filament wound composite cylinders under external pressure, Compos. Sci. Technol. 68 (3–4) (2008) 1015–1024, http://dx.doi.org/10.1016/j.compscitech.2007.07.020.

[18] H.H. Mian, H. Rahman, Influence of mosaic patterns on the structural integrity of filament wound composite pressure vessels, Int. J. Struct. Integr. 2 (3) (2011) 345–356, http://dx.doi.org/10.1108/17579861111162932.

[19] W. Wen, J. Li, H. Cui, Y. Xu, H. Zhang, Experimental research on failure of filament wound composite pipe under axial tension, Appl. Mech. Mater. 268 (PART 1) (2013) 74–77, http://dx.doi.org/10.4028/www.scientific.net/AMM.268-270.74.

[20] Z. Guo, Z. Li, J. Cui, Y. Li, Y. Luan, The effect of winding patterns on the mechanical behavior of filament-wound cylinder shells, Multidiscip. Model. Mater. Struct. 16 (3) (2020) 508–518, http://dx.doi.org/10.1108/MMMS-03-2019-0059.

[21] P. Stabla, M. Smolnicki, W. Błażejewski, The numerical approach to mosaic patterns in filament-wound composite pipes, Appl. Compos. Mater. 28 (1) (2021) 181–199, http://dx.doi.org/10.1007/s10443-020-09861-z.

[22] P. Stabla, M. Lubecki, M. Smolnicki, The effect of mosaic pattern and winding angle on radially compressed filament-wound CFRP composite tubes, Compos. Struct. 292 (July 2022) (2022) http://dx.doi.org/10.1016/j.compstruct.2022.115644.

[23] T.V. Lisbôa, J.H.S. Almeida Jr., A. Spickenheuer, M. Stommel, S.C. Amico, R.J. Marczak, FEM updating for damage modeling of composite cylinders under radial compression considering the winding pattern, Thin-Walled Struct. 173 (2022) 108954, http://dx.doi.org/10.1016/j.tws.2022.108954.

[24] S.G. Castro, J.H.S. Almeida Jr., L. St-Pierre, Z. Wang, Measuring geometric imperfections of variable–angle filament–wound cylinders with a simple digital image correlation setup, Compos. Struct. 276 (2021) 114497, http://dx.doi.org/10.1016/j.compstruct.2021.114497.

[25] M. Torres Arellano, L. Crouzeix, B. Douchin, F. Collombet, H. Hernández Moreno, J. González Velázquez, Strain field measurement of filament-wound composites at ±55° using digital image correlation: An approach for unit cells employing flat specimens, Compos. Struct. 92 (10) (2010) 2457–2464, http://dx.doi.org/10.1016/j.compstruct.2010.02.014.

[26] ANSYS Mechanichal Enterprise, Release 2021.1, 2021.

[27] D.N. Arnold, R.S. Falk, Analytical and Computational Models for Shells, American Society of Mechanical Engineers, New York, 1989.

[28] D. Scida, Z. Aboura, M. Benzeggagh, E. Bocherens, Prediction of the elastic behaviour of hybrid and non-hybrid woven composites, Compos. Sci. Technol. 57 (12) (1998) 1727–1740, http://dx.doi.org/10.1016/S0266-3538(97)00105-X.

[29] J.T. da Rocha, T.V. de Lisboa, R.J. Marczak, The influence of weaving patterns on the effective mechanical response of reinforced composites - A study through homogenization, in: A.B. Jorge, C.T.M. Anflor, G.F. Gomes, S.H.S. Carneiro (Eds.), Fundamental Concepts and Models for the Direct Problem, Vol. II, University of Brasilia Central Library, 2022, pp. 76–119.